An adaptive reduced order model for the angular discretisation of the Boltzmann transport equation using independent basis sets over a partitioning of the space-angle domain

Alexander C. Hughes[1] and Andrew G. Buchan[1]

[1]School of Engineering and Materials Science, Queen Mary University of London, London, UK

April 21, 2022

Abstract

This article presents a new reduced order model (ROM) for the angular discretisation of the Boltzmann transport equation. The angular ROM is built over a partitioning of the space-angle phase-space, by generating independent, optimised angular basis function sets for each partition. The advantage is that each basis function set is optimised to represent the neutron flux distribution in a particular partition of space and angle, rather than being optimised for the entire domain. This serves to reduce the total number of basis functions required, and therefore the solve time. Two numerical examples are presented to demonstrate the efficacy of the methods - a dog-leg duct problem, involving particle streaming, and the Watanabe-Maynard problem, which includes significant particle scattering. In both cases, it is shown that the method reduces the angular flux error, for a given basis size or solve time, by around an order of magnitude in comparison to other, similar ROM methods. An adaptive version of the method is also presented, whereby the number of basis functions within each space-angle partition can vary independently. It is shown to potentially provide further significant reductions in error.

1 Introduction

Numerical and mathematical models play an essential role in the analysis of many systems across a wide range of fields in science and engineering. They are utilised extensively in the nuclear sector, where they are essential tools for design and analysis. For example, they can be applied to predict neutron population distributions [1], radiation intensities [2], and the flows of coolant and heat within reactor cores [3]. For complex problems, numerical models can require significant computational resources due to the scale of the problems and the

high dimensionality of the equations involved. For example, reactor cores are constructed from many tens of thousands of fuel and control rods, so large spatial meshes are required to resolve their full domain. Furthermore, predicting the distribution of neutrons within cores accurately involves solving the Boltzmann transport equation (BTE), which has a 7-dimensional phase-space.

Over the years, many articles have been published which focus on the formulation of efficient solutions to the BTE, such as the use of self-adaptive methods [4, 5, 6] which reduce the total degrees of freedom by distributing resolution efficiently - that is, only where it is beneficial. However, over the last decade reduced order methods (ROMs) have gained popularity, as they are capable of forming and applying basis functions which are optimised for a particular class of problem. They have been demonstrated to reduce problem sizes by orders of magnitude, resulting in a similar scale of reductions to solve times.

ROMs have been applied extensively across many fields of engineering. Recent developments include the application of proper orthogonal decomposition (POD) to transient heat conduction [7], turbulent supersonic jets [8], acoustic waves [9], incompressible magneto-hydrodynamics [10], and many other problems. POD-based methods have been combined with neural networks to model plasticity [11], unsteady flows in a combustion problem [12], the viscous Burgers equation [13], and structural damage [14]. Purely neural network-based ROMs have also been implemented, with applications including the modelling of biomass fast pyrolysis [15] and pH reactors [16]. Many other model order reduction strategies have been developed, including the Volterra [17] and Fourier [18] series expansions, space mapping [19], the Kriging [20] and harmonic balance [21] methods, and radial basis functions [22]. Related to the work of this article, ROMs have also been developed that use and apply basis functions over a domain decomposition, or localised regions of a problem. These have been used to solve advection-diffusion problems [23], Maxwell's equations [24], the Stokes equations [25], and elliptic multi-scale problems. Mixed approaches have also been described using both high-order methods and reduced order models over a domain decomposition, applying ROMs over regions that they can resolve well, with high order methods used elsewhere. Applications include solutions to the Laplace equations [26] and, more recently, the compressible Euler equations [27].

The field of nuclear engineering and general radiation transport simulation, has made use of ROMs to solve a variety of problems. Early examples of ROMs in the field include [28], which used several ROM techniques to analyse the transient dynamics of reactor-driven systems; [29], which applied them to one dimensional transient radiation problems; and [30], which applied POD to the spatial dimensions of eigenvalue problems in the context of reactor physics. Further developments include the application of POD to the angular dimension of the BTE [31, 32, 33], space-angle ROMs for radiative heat transfer [34], and the use of range-finding algorithms for the linear transformation of parameters in multiphysics problems [35]. More recently, POD has been used to model fuel burnup [36] and reactor power distributions [37]. Many articles have also considered the problem of control rod movement using various ROMs, including early work based on proper generalised decomposition [38], and recent publications which employed POD [39], the empirical interpolation method [40], and neural networks [41].

Recently, a new adaptive POD method known as discontinuous POD (DPOD) was developed, which applied angular POD functions to optimally resolve the angular dimension of

the BTE over distinct partitions of the angular domain [42]. The method was demonstrated to create stable basis sets which provided efficient solutions to multi-dimensional transport problems. In this article, a simple but highly effective new modification is presented to extend this capability, in order to improve the efficiency of the method by further reducing the dimensionality of problems. Known here as regional discontinuous POD (RDPOD), the new model forms and applies independent sets of angular basis functions, which are each optimised to resolve different partitions of the space-angle phase-space of the BTE. That is, the method forms separate angular POD functions over distinct regions of space, rather than using a single basis set for all regions of space as developed in the previous method [42]. Whilst this is a simple modification, it is of particular importance as the neutron flux distribution often varies substantially over space and angle. Capturing the characteristics of the neutron flux using a single set of basis functions can therefore place high demands on the original ROM formulation. Partitioning the spatial and angular dimensions and creating separate anguar ROMs for each partition can help to overcome this issue. As the variation in neutron flux distributions within each partition is considerably smaller than the variation across the entire problem, the number of basis functions required to resolve each distribution is reduced substantially. This can lead to smaller systems of equations, and therefore reduce solve times.

While there has been a large amount of research interest in developing ROMs which are localised over decomposed domains, this is the first to do so using angular basis functions to resolve the BTE. Furthermore, this article presents an implementation of angular adaptivity for the RDPOD basis sets, adaptive RDPOD (ARDPOD), which allows the number of RDPOD basis functions to appropriately vary between space-angle partitions. In addition, this article presents a method which enables the efficient transfer of information between regions with different angular basis sets.

The capabilities of these ROMs are demonstrated with two problems - one involving only advection and absorption, and another which also includes scattering. It is shown that the reduction in basis sizes and solve times for a given error can exceed an order of magnitude in comparison to previous work on angular ROMs [31, 42]. Further significant improvements were achieved through the use of adaptive resolution, which reduced error by up to 2 orders of magnitude compared to the non-adaptive method in some cases. Whilst these reductions are already significant, perhaps their benefits would be greater still when applied to large-scale reactor physics problems with far greater levels of variation in their neutron flux distributions.

The sections of this article are arranged as follows. Section 2 presents the BTE together with its general angular and spatial discretisations. Section 3 presents the development of the ROM, and describes the communication between different basis sets, as well as the adaptive angular resolution procedure. Section 4 presents two numerical examples which demonstrate the capabilities of each method. Section 5 completes the article by presenting its conclusions.

2 The Boltzmann Transport Equation and Space-Angle Discretisation

The steady-state, mono-energetic Boltzmann transport equation governs the angular flux $\psi(\vec{r}, \Omega)$ in direction Ω at position $\vec{r}$,

$$\Omega \cdot \nabla\psi(\vec{r}, \Omega) + \Sigma_t(\vec{r})\psi(\vec{r}, \Omega) = q_{ex}(\vec{r}) + \int_{\Omega'} \Sigma_s(\vec{r}, \Omega' \rightarrow \Omega)\psi(\vec{r}, \Omega')d\Omega'. \tag{1}$$

The first term in equation 1 is the advection operator; the second is the removal term, which accounts for losses from both absorption and scattering; the third denotes the isotropic external source; and the fourth represents the scattering into the angle Ω from all angles Ω'. The macroscopic scattering and total removal cross sections are given by Σ_s and Σ_t, respectively. The symbols in brackets indicate the continuous dimensions associated with each variable - $\vec{r}$ and Ω for spatial and angular continuity, respectively.

2.1 Angular Discretisation of the Boltzmann Transport Equation

As the process of discretisation closely follows that of [42], only a summary is presented here. The Galerkin method is applied to discretise the angular dimension of equation 1. The angular flux $\Psi(\vec{r}, \Omega)$ is approximated by a sum of N_a angular basis functions $\mathcal{G}_j(\Omega)$ multiplied by the coefficients $\psi_j(\vec{r})$,

$$\psi(\vec{r}, \Omega) \approx \sum_{j=1}^{N_a} \mathcal{G}_j(\Omega)\psi_j(\vec{r}). \tag{2}$$

The approximation in equation 2 is inserted into equation 1, which is then weighted and integrated over all angles. The basis functions $\mathcal{G}$ are also used as weighting functions. Thus equation 1 is expressed in the angularly discretised form,

$$(\mathbf{A} \cdot \nabla + H(\vec{r}))\Psi(\vec{r}) = Q(\vec{r}), \tag{3}$$

where $\mathbf{A}$ is a vector of matrices (A_x, A_y, A_z), each containing the components of the unit vectors Ω in the corresponding Cartesian axis. The removal and scattering terms are grouped into the matrix H. The coefficients of the angular expansion are contained in the vector $\Psi(\vec{r})$, and the angularly discretised source term is represented by the vector $Q(\vec{r})$. All matrices are of size $N_a \times N_a$, and all vectors besides $\mathbf{A}$ are of size N_a. The components of each matrix and vector in equation 3 are given in [42].

Each class of problem is resolved using the discrete ordinates (S_N) method for n_p cases with varying conditions, such as perturbations to the nuclear material cross-sections. The vectors of S_N angular coefficients are partitioned into sets according to the angular octant Ω_q of each angle,

$$\Psi(\vec{r}) = \begin{bmatrix} \Psi_1(\vec{r}) \\ \vdots \\ \Psi_q(\vec{r}) \\ \vdots \\ \Psi_8(\vec{r}) \end{bmatrix}, \tag{4}$$

where $\Psi_q(\vec{r})$ is a vector containing the $N_a/8$ coefficients with associated directions within the octant Ω_q.

2.2 Spatial Discretisation of the Boltzmann Transport Equation

The discontinuous Galerkin finite element method is applied to discretise the spatial dimensions of the BTE [42, 43]. The angularly discretised flux $\Psi(\vec{r})$ in equation 3 is approximated as a sum of the N_s spatial basis functions $\mathcal{N}_j(\vec{r})$ multiplied by the coefficients Ψ_j,

$$\Psi(\vec{r}) \approx \sum_{j=1}^{N_s} \Psi_j \mathcal{N}_j(\vec{r}). \tag{5}$$

This approximation is inserted into equation 3, which is then converted to its weak form by weighting with the set of basis functions $\mathcal{N}(\vec{r})$ and integrating over the volume of each element, V_e. Green's theorem is applied to the advection term, splitting it into an integral over V_e and another over the element boundary Γ_e. Finally, the boundary term is split into inflow and outflow components, as first order upwinding is used to calculate the flow at element boundaries [5, 44]. The result is a full order discretised formulation of the BTE,

$$\begin{aligned}\sum_{j=1}^{N_s} \Bigg\{ \Big(-\int_{\mathrm{V}_e} \nabla \mathcal{N}_i(\vec{r}) \mathbf{A} \mathcal{N}_j(\vec{r}) d\mathrm{V} + \int_{V_e} \mathcal{N}_i(\vec{r}) H(\vec{r}) \mathcal{N}_j(\vec{r}) d\mathrm{V} \Big) \Psi_j \\ + \int_{\Gamma_e} \mathcal{N}_i(\vec{r}) (\mathbf{A}^{in} \cdot \hat{n}) \mathcal{N}_j(\vec{r}) d\Gamma_e \Psi_j^{in} + \int_{\Gamma_e} \mathcal{N}_i(\vec{r}) (\mathbf{A}^{out} \cdot \hat{n}) \mathcal{N}_j(\vec{r}) d\Gamma_e \Psi_j^{out} \Bigg\} \\ = \int_{\mathrm{V}_e} \mathcal{N}_i(\vec{r}) Q(\vec{r}) d\mathrm{V}, \\ \forall i \in \{1, N_s\}, \end{aligned} \tag{6}$$

where $\hat{n}$ is the unit vector normal to the element boundary; Ψ_j^{out} is the outflow, given by the angular flux vector of the element in question; and Ψ_j^{in} is the inflow, given by the angular flux vectors of the element's upstream neighbours. The matrices $A^{in} = (\mathbf{A}^{in} \cdot \hat{n})$ and $A^{out} = (\mathbf{A}^{out} \cdot \hat{n})$ are formed to pass the correct incoming and outgoing information, respectively, through the element's surface. For S_N, they are produced by simply retaining the negative and positive diagonal elements, respectively, of the matrix $(\mathbf{A} \cdot \hat{n})$. In the general case, a Riemann approach can be employed [45]. Equation 6 gives the general form of the BTE after discretisation in both space and angle, and can therefore be applied to any arbitrary angular approximation.

3 The Discontinuous Angular Reduced Order Model

This section presents a new angular POD method that forms independent angular basis sets which are each optimised to resolve a specific partition of the space-angle phase-space of the

BTE. The angular domain Ω and spatial domain V are partitioned into the two sets,

$$\Omega = \bigcup_{q=1}^{8} \Omega_q \qquad \text{and} \qquad V = \bigcup_{r=1}^{n_r} V_r, \tag{7}$$

where Ω_q and V_r represent subsets of the angular and spatial domains, respectively, as illustrated in figure 1. The DPOD method described in [42] corresponds to the use of a single spatial region spanning the domain, that is, n_r=1. If a single angular partition spanning the full sphere is also used, then the standard angular POD method described in [31] is recovered.

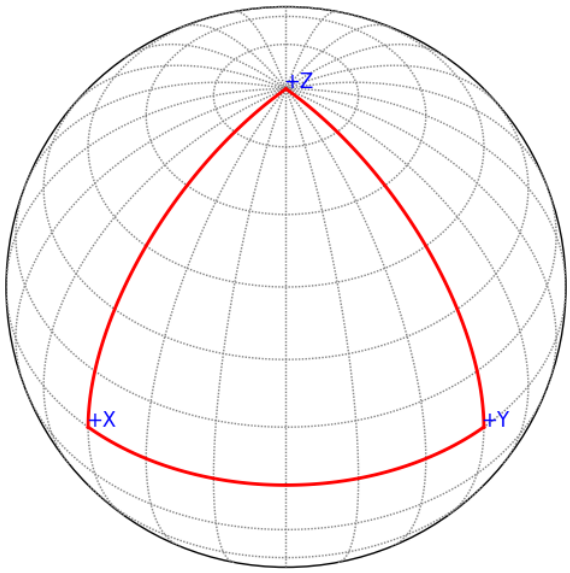

(a) An angular octant on the sphere. The red lines delimit the boundaries. Each basis function is non-zero in one out of eight octants.

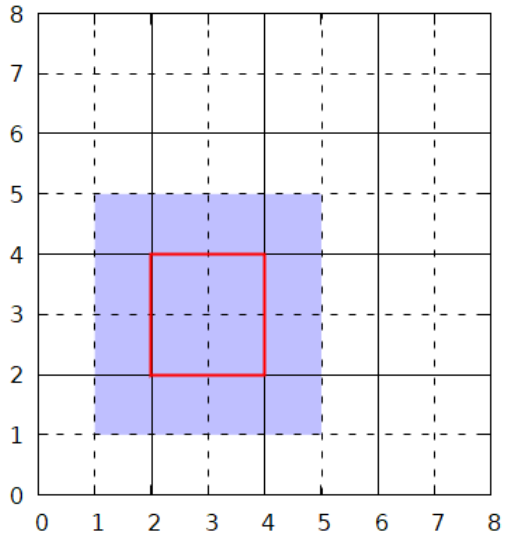

(b) A spatial region within an 8x8 element domain, using 4x4 regions. Dashed black lines are element boundaries, solid black lines are element and region boundaries, and the red square encloses the region which takes snapshots from all elements shaded blue.

Figure 1: The spatial and angular discontinuities imposed by the RDPOD method.

In line with the DPOD method, the angular domain is partitioned into 8 octants. Each spatial partition may in principle contain any arbitrary set of n_r elements in the spatial domain. A cross-product of the two partitions in equation 7 forms the space-angle partition of the complete phase-space, which is given by,

$$Z = \bigcup_{q,r} Z_{q,r}, \tag{8}$$

where the phase-space partition spanning the angular octant Ω_q and spatial region V_r is denoted $Z_{q,r}$.

The POD functions are formed for each partition via the method of snapshots [46]. The angular coefficients from the S_N model are used to form the snapshot matrices for each partition. The angular coefficient vectors Ψ are partitioned by octant as shown in equation

4, and each component Ψ_q is assigned to a spatial region V_r based on its position. Separate snapshot matrices $S_{q,r}$ are formed for each partition $Z_{q,r}$, resulting in $8 \times n_r$ matrices.

The snapshot matrices $S_{q,r}$ also include vectors of angular coefficients from the elements adjacent to V_r, as this helps to preserve information when mapping between regions. This is shown in figure 1b, where the region enclosed in red takes snapshots from all elements shaded in blue. For each $Z_{q,r}$, the associated snapshot set is therefore defined as,

$$S_{q,r} = \begin{bmatrix} | & | & & | \\ \Psi_{q,r,1} & \Psi_{q,r,2} & ... & \Psi_{q,r,n_s} \\ | & | & & | \end{bmatrix}, \qquad \forall q \in \{1,8\}, \forall r \in \{1,n_r\}, \tag{9}$$

where each $\Psi_{q,r,i}$ is a vector of size $N_a/8$ containing the angular coefficients of the ith snapshot associated with the partition $Z_{q,r}$. The term n_s, which may vary for each snapshot set, denotes the total number of snapshots in $S_{q,r}$. This is given by $n_s = N_r \times N_p$, where N_r is the number of FEM basis nodes in partition V_r, including the neighbouring nodes as shown in blue in figure 1b, and N_p is the number of problem variations used to train the ROM.

The RDPOD basis sets for each $Z_{q,r}$ can now be formed through the SVD of each snapshot matrix,

$$S_{q,r} = \mathrm{U}_{q,r}\Sigma_{q,r}\mathrm{V}_{q,r}^T, \tag{10}$$

where $\mathrm{U}_{q,r}$ and $\mathrm{V}_{q,r}$ are unitary matrices of sizes $N_a/8 \times N_a/8$ and $n_s \times n_s$, respectively. The column vectors of $\mathrm{U}_{q,r}$ contain the optimised basis vectors that best represent the snapshot data, ordered such that the first n_a columns form the optimal n_a basis vectors in the Frobenius norm. Here, n_a is the same for all q and r, though this is not required. A method for varying the number of basis functions by region and octant is described in section 3.1. The RDPOD basis matrices $\mathcal{U}_{q,r}$ are formed by truncating each snapshot matrix such that only the first n_a columns are retained. The fraction of the information in $\mathrm{U}_{q,r}$ which is retained in $\mathcal{U}_{q,r}$ can be determined from the singular values,

$$I_{q,r} = \frac{\sum_{i=1}^{n_a}(\Sigma_{q,r,i,i})^2}{\sum_{i=1}^{N_a}(\Sigma_{q,r,i,i})^2}, \tag{11}$$

where $I_{q,r}$ varies from 0 to 1, with 1 being total capture of the snapshot information. The matrices $\mathcal{U}_{q,r}$ can be used to map the angular coefficients between the full and reduced order models through the relationship,

$$\Psi_{q,r} \approx \mathcal{U}_{q,r}\alpha_{q,r}, \qquad \forall q \in \{1,8\}, \forall r \in \{1,n_r\}, \tag{12}$$

where $\alpha_{q,r}$ contains a vector of n_a coefficients of $\mathcal{U}_{q,r}$, for each node within $\mathrm{Z}_{q,r}$. The combined mapping over all angular partitions in each region V_r can be expressed as,

$$\mathcal{U}_r\alpha_r = \begin{bmatrix} \mathcal{U}_{1,r} & 0 & 0 & 0 & 0 \\ 0 & \ddots & 0 & 0 & 0 \\ 0 & 0 & \mathcal{U}_{q,r} & 0 & 0 \\ 0 & 0 & 0 & \ddots & 0 \\ 0 & 0 & 0 & 0 & \mathcal{U}_{8,r} \end{bmatrix} \begin{bmatrix} \alpha_{1,r} \\ \vdots \\ \alpha_{q,r} \\ \vdots \\ \alpha_{8,r} \end{bmatrix} = \begin{bmatrix} \mathcal{U}_{1,r}\alpha_{1,r} \\ \vdots \\ \mathcal{U}_{q,r}\alpha_{q,r} \\ \vdots \\ \mathcal{U}_{8,r}\alpha_{8,r} \end{bmatrix}, \qquad \forall r \in \{1,n_r\}. \tag{13}$$

Equations 4 and 12 enable this to be compactly written as,

$$\mathcal{U}_r \alpha_r(\vec{r}) \approx \Psi(\vec{r}), \tag{14}$$

which holds for any spatial position $\vec{r}$ inside region r.

Substituting equation 14 into equation 3 and premultiplying by $\mathcal{U}_r^T$ projects the angularly discretised equations onto the POD space. This projection is applied to each region V_r separately,

$$\mathcal{U}_r^T(\mathbf{A}\cdot\nabla + H(\vec{r}))\mathcal{U}_r\alpha_r(\vec{r}) = \mathcal{U}_r^T Q(\vec{r}), \qquad \forall r \in \{1, n_r\}. \tag{15}$$

Equation 15 is then spatially discretised as described in section 2.1, resulting in the fully discretised RDPOD formulation of the BTE.

The spatially discretised forms of equation 15, equivalent to projections of equation 6 onto the RDPOD bases, are constructed separately for each spatial partition V_r using their own optimised RDPOD angular basis sets. Communication between the elements within each partition, and between neighbouring partitions, is implemented through the surface integrals of equation 6. As mentioned, a Riemann approach can be employed to form the incoming and outgoing matrices inside the surface integrals for a general angular discretisation. They can also be obtained through pre- and post-multiplication of the full order matrices A^{in} and A^{out} by the RDPOD mapping matrices $\mathcal{U}_r^T$ and $\mathcal{U}_r$. For adjacent elements within the same region V_r, the incoming and outgoing surface matrices of equation 6 are given by,

$$A^{in} = \mathcal{U}_r^T A^{in} \mathcal{U}_r, \qquad \text{and} \qquad A^{out} = \mathcal{U}_r^T A^{in} \mathcal{U}_r, \tag{16}$$

respectively. To obtain an element's incoming surface information from an adjacent element belonging to a different region, say $V_{r'}$, one must use the correct mapping to account for the fact that the incoming vector employs a different RDPOD basis. This is simply achieved by mapping the RDPOD coefficients $\alpha_{r'}$ from the incoming element to the full model space, applying the (S_N) incoming advection operator, then projecting the resulting vector onto the basis of region V_r. That is, the incoming advection matrices in the RDPOD formulation are given by,

$$A^{in}_{r,r'} = \mathcal{U}_r^T A^{in} \mathcal{U}_{r'}. \tag{17}$$

The matrices $A^{in}_{r,r'}$ are precomputed for each pair of regions r and r' with a common border. They can then be employed in equation 6, where the incoming surface integral can be explicitly written as,

$$\sum_{j=1}^{N_s} \int_{\Gamma_e} \mathcal{N}_i(\vec{r}) A^{in}_{r,r'} \mathcal{N}_j(\vec{r}) d\Gamma_e \alpha^{in}_{r',j}, \qquad \forall i \in \{1, N_s\}. \tag{18}$$

As stated previously, in the case of a single spatial region spanning the domain, the DPOD method presented in [42] is recovered. Using a single spatial region together with a single angular region spanning the sphere, the original angular POD method in [31] is recovered.

3.1 Adaptivity in Angle

This section presents an adaptive algorithm using the RDPOD basis functions, known as adaptive RDPOD (ARDPOD). Instead of utilising the same number of basis functions n_a

throughout the domain, each partition $Z_{q,r}$ has an associated number of basis functions $n_{q,r}$, which can be modified independently. The adaptive algorithm uses an error metric to estimate the effect of increasing $n_{q,r}$ for each $Z_{q,r}$, and adds basis functions where they are likely to minimise the total error.

The contribution of each basis function to the solution is dependent only on the magnitudes of its coefficients. The basis functions form a hierarchical set, which implies that the coefficients of each successive function will tend towards zero as the approximation converges. It can thus be inferred that additional basis functions are likely to be most beneficial in partitions where the coefficient of the final basis function currently included is large. However, successive coefficients have been observed to oscillate between positive and negative about zero, and so a single small coefficient does not guarantee convergence. The error metric therefore considers the final two coefficients.

An initial solution is required in order to calculate the error metric and begin the adaptive process, and so the problem in question is first solved with,

$$n_{q,r} = 2, \qquad \forall q \in \{1, 8\}, \forall r \in \{1, n_r\}. \tag{19}$$

Next, the relative contribution from the final two basis functions is calculated for each partition $Z_{q,r}$,

$$\mathrm{F}_{q,r} = \frac{(\alpha_{q,r,n_{q,r}-1} + \alpha_{q,r,n_{q,r}})}{\sum_{q=1}^{8} \sum_{r=1}^{n_r} \sum_{i=1}^{n_{q,r}} \alpha_{q,r,i}}, \qquad \forall q \in \{1, 8\}, \forall r \in \{1, n_r\}, \tag{20}$$

where $\alpha_{q,r,i}$ denotes the i^{th} angular coefficient in the partition $Z_{q,r}$. A threshold value τ is set to some inital, relatively large value, typically 1. A variable known as the threshold divisor, δ_τ, is set to some value greater than 1. In this article, $\delta_\tau = 2$. Each iteration, basis functions are added according to the equation,

$$n_{q,r} = n_{q,r} + 1, \qquad \forall\ (q, r) \in \{\ (q', r') \mid \mathrm{F}_{q',r'} > \tau\}. \tag{21}$$

The number of basis functions added in this process, n_Δ, is counted and compared to the minimum number of basis functions to add per iteration, n_+. If $n_\Delta < n_+$, then $\tau = \tau/\delta_\tau$ and equation 21 is applied again with the new value of τ. The process repeats until $n_\Delta > n_+$, at which point the next iteration can begin. Once $n_{q,r}$ has been adjusted, the process repeats until a desired number of basis functions is reached. The complete adaptive method is described by algorithm 1.

Algorithm 1: Adaptive RDPOD

```
n_{q,r} = 2 for all q and r.
/* Iterate until the desired number of basis functions is reached.   */
while sum(n_{q,r}) < maximumBasisFunctions do
    Solve the ROM.
    Calculate F_{q,r}.
    n_Δ = 0;
    while n_Δ < n_+ do
        /* Loop through partitions and add basis functions.          */
        for q = 0 to 8 do
            for r = 0 to n_r do
                if F_{q,r} > τ then
                    n_{q,r} += 1;
                    n_Δ += 1;
                end
            end
        end
        /* Decrease the threshold value τ if necessary.              */
        if n_Δ < n_+ then
            τ = τ/δ_τ;
        end
    end
end
```

4 Numerical Examples

In this section, two numerical examples are presented in order to compare performance of DPOD, RDPOD and ARDPOD. Uniform quadrilateral FEM spatial meshes are employed, using discontinuous bilinear basis functions. The full order method employs the S_N discretisation, with a sufficiently high angular resolution to ensure that the solutions have converged in angle.

A sweep based solver is employed for all methods, which solves for the unknowns of each mesh element in turn, following the path of information flow. Standard sweeping is employed for the full order model, where each ray is resolved individually and elements visited in the order of information flow along the direction of the ordinate [47, 48]. For the ROMs, as the angular coefficients are heavily coupled, all angular coefficients are solved simultaneously for each element. Four sweep directions are used for the two dimensional problems presented here when structured meshes are applied. Elements are swept from left to right, top to bottom (and then in reverse), and top to bottom, left to right (and then in reverse). However, the focus of this article is not on developing the most efficient solver technology to resolve the various angular models. In fact, there are several ways to increase efficiency, but each would require substantial development and warrant a separate article. So, whilst solver times are provided, these should be considered conservative estimates, and it is highly likely that reductions can and will be made in future. Thus the main purpose of

this analysis is to demonstrate the methods' increased accuracy for a given basis size when compared with DPOD, which has previously been demonstrated to outperform both S_N and standard angular POD by the same metric [42].

In the examples presented, the spatial partitions used to construct the ROMs are of regular structure, despite equation 8 allowing for any arbitrary partitioning to be used. Whilst the ideal implementation would minimise the variation in angular flux profiles within each partition, generating partitions in this manner would require significant additional work. This article will instead focus on demonstrating that even regularly shaped partitions can drastically improve modelling efficiency. This demonstration therefore forms a foundation for future work on the generation of optimal partitions for further improvements to efficiency.

Finally, it is sufficient to say that the ROM's computer memory requirements are relatively small. The memory usage increases linearly with the number of regions, n_r, since each sub-region requires its own set of discretised angular matrices. However, as shown in the numerical examples, the angular size of the reduced system should be typically small, on the order of a few tens. Thus, taking a large angular ROM of size, say, 100, and using a reasonably large set of partitions, say, $n_r = 1000$, a matrix free solver would require less than 0.6 GiB RAM. Clearly, if parts of the matrix resulting from the spatially discretised equations had to be stored then the memory requirements would increase substantially. Whilst a matrix-free solver is most desirable to avoid large memory requirements, particularly for unstructured finite element meshes, this has yet to be developed. In this article, a uniform structured mesh is used, which enables a single element-wise discretised matrix (from the element-wise discretised equations 6) to be stored for each partition. Again using the example of 1000 partitions and 100 angular POD functions, only 1.5 GiB of memory is required for storage in this case.

4.1 The Dog-Leg Duct Problem

The first example is a dog-leg duct problem [49]. Figure 2a shows a schematic of the domain. Region 1 is a source, region 2 is the duct, and region 3 is a heavy absorber. Vacuum boundary conditions are applied to the top and right boundaries, and reflective boundary conditions to the bottom and left boundaries. The spatial domain is discretised with a 140×180 mesh of discontinuous linear quadrilateral elements. The full order solutions used for snapshots and error calculations employed the S_{50} angular discretisation. Figure 2b shows the scalar flux distribution of the S_{50} solution to the interpolation problem.

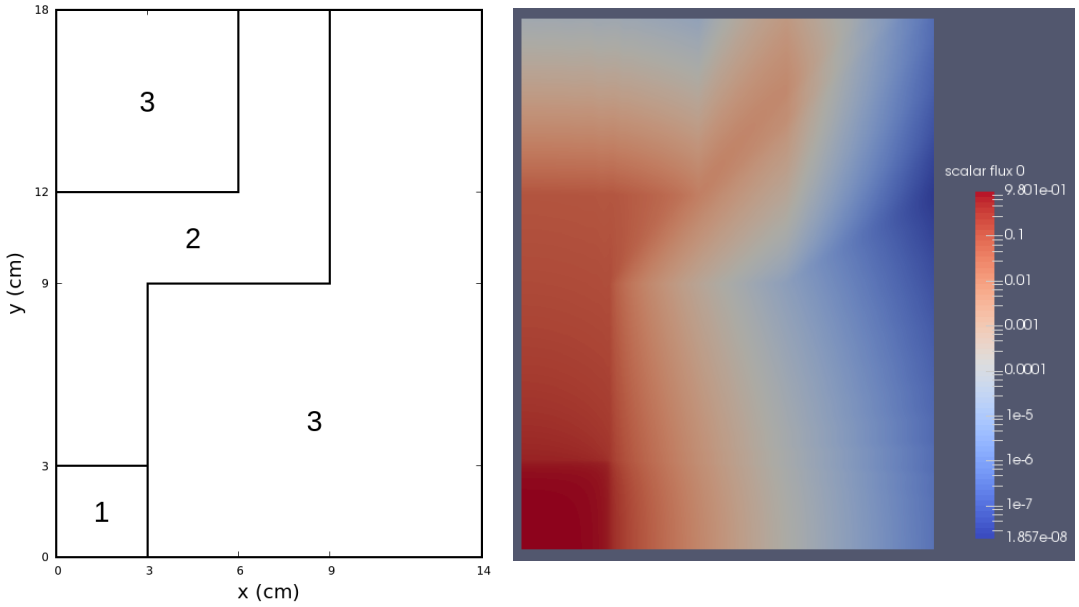

(a) Dog-leg duct schematic

(b) S_{50} scalar flux solution to interpolation problem

Figure 2: Schematic (a) and S_{50} scalar flux solution (b) for the dog-leg duct interpolation problem. Region 1 is the source, region 2 is the duct, and region 3 is a highly absorbing material.

Table 1 lists the material cross sections for the training and test problems. The snapshot matrix was formed from all four training solutions, and the resulting RDPOD bases were used to solve the test problems. The first test problem is referred to as the *interpolation* problem, as its material properties are within the range for which snapshots were produced, and the second is referred to as the *extrapolation* problem, as its material properties lie outside of this range.

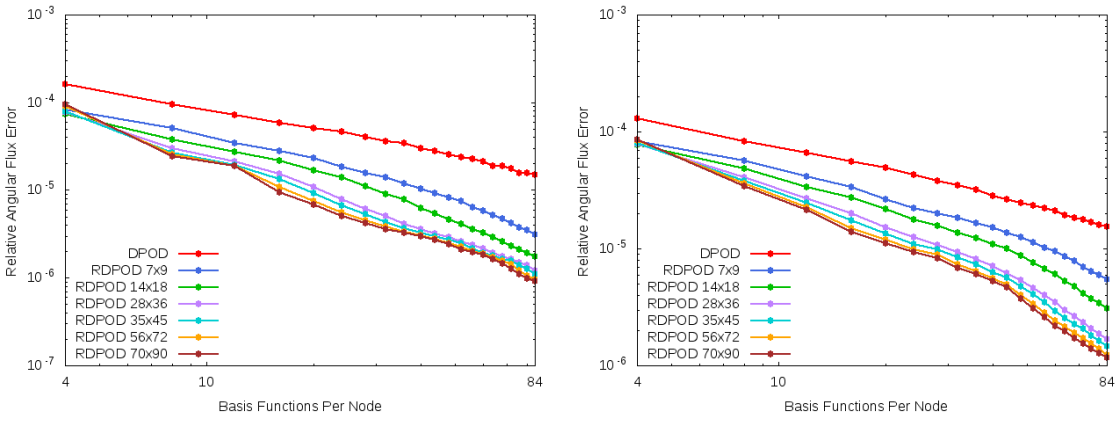

(a) Interpolation

(b) Extrapolation

Figure 3: Angular flux error vs number of basis functions for S_{50} solutions to the dog-leg duct problems with varying numbers of spatial regions. "$a \times b$" indicates a spatial partitions in x and b in y, for a total of $a \times b$.

Figure 3 compares the L^2-norms of the relative angular flux errors for the dog-leg duct

interpolation and extrapolation problems using DPOD and RDPOD, with varying numbers of basis functions and regions. The results show that RDPOD consistently reduces error compared to DPOD for a given angular basis size. Furthermore, increasing the number of spatial partitions consistently reduces the error. For the largest set of spatial partitions, the error is reduced by approximately 1 order of magnitude with 16 basis functions. The reduction in error compared to DPOD continues to grow as the angular resolution is increased further.

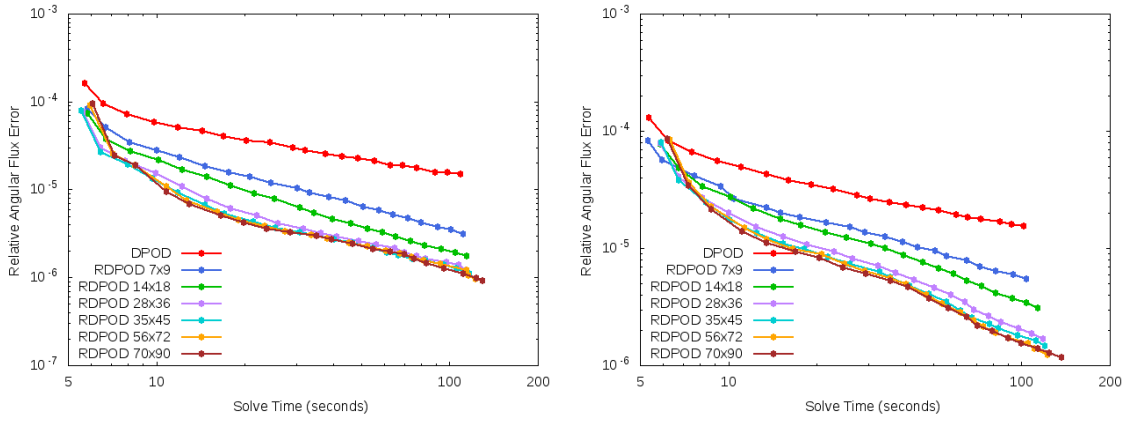

(a) Interpolation (b) Extrapolation

Figure 4: Angular flux error vs solve time in seconds for S_{50} solutions to the dog-leg duct problems with varying numbers of spatial regions. "$a \times b$" indicates a spatial partitions in x and b in y, for a total of $a \times b$.

Figure 4 presents the L^2-norm of the relative angular flux error against the solve time for both interpolation and extrapolation problems, for varying numbers of basis functions and regions. Similar trends are observed, with RDPOD reducing the solve time required to achieve a given error. For the largest spatial partition sets, the solve times are reduced by over an order of magnitude with a relative error of around 10^{-5}. The trends in the graph indicate that greater efficiency will be achieved for lower error tolerances.

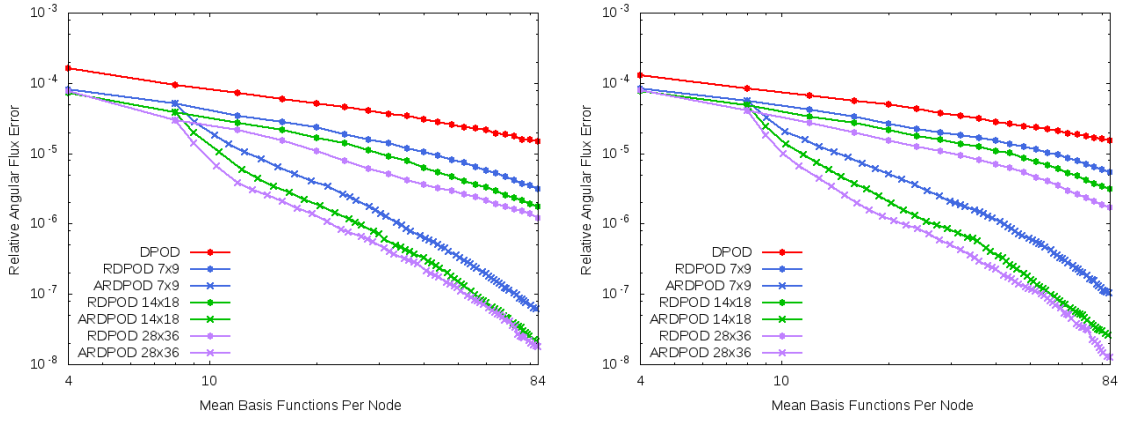

(a) Interpolation (b) Extrapolation

Figure 5: Angular flux error vs number of basis functions for S_{50} solutions to the dog-leg duct problems with varying numbers of spatial regions using angular adaptivity.

Figure 5 presents the relative angular flux error vs the mean number of basis functions per node for DPOD, and for RDPOD and ARDPOD with varying numbers of regions. It is shown that ARDPOD significantly reduces the error for a given angular basis size. With just 12 basis functions, the error was reduced by approximately half an order of magnitude compared to RDPOD, and by more than an order of magnitude compared to DPOD. By 84 basis functions, the reductions in error for a given basis size had increased to almost 2 orders of magnitude compared to RDPOD and approximately 2.5 orders of magnitude compared to DPOD.

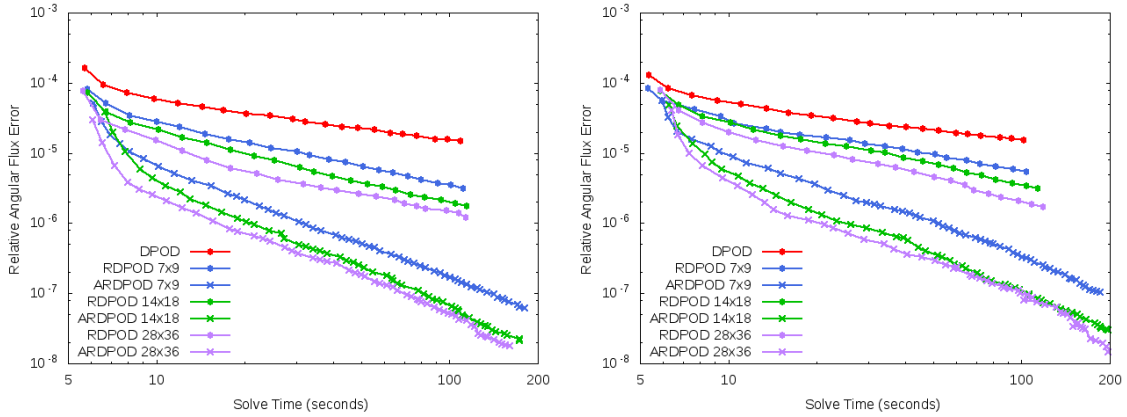

(a) Interpolation

(b) Extrapolation

Figure 6: Angular flux error vs solve time in seconds for S_{50} solutions to the dog-leg duct problems with varying numbers of spatial regions using angular adaptivity. "$a \times b$" indicates a spatial partitions in x and b in y, for a total of $a \times b$.

Figure 6 presents the relative angular flux error against the solve time for DPOD, RDPOD and ARDPOD. The adaptive solve times show the time taken to complete the final iteration of the adaptive process, starting from a zero solution. This gives an indication of the performance of ARDPOD once the adaptive stage is complete and an efficient basis function distribution has been generated. It is shown that the adaptive method drastically reduces the solve time required to reach a given level of error in comparison to both DPOD and RDPOD. At around 20 seconds of solve time, the ARDPOD errors are reduced by just over an order of magnitude in comparison to RDPOD, and by around 2 orders of magnitude when compared to DPOD.

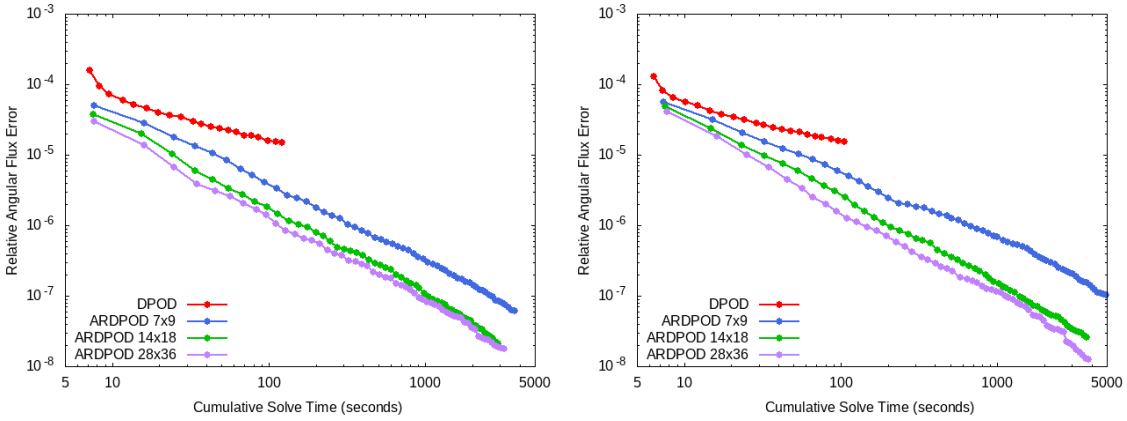

(a) Interpolation

(b) Extrapolation

Figure 7: Angular flux error vs cumulative solve time in seconds for S_{50} solutions to the dog-leg duct problems with varying numbers of spatial regions using angular adaptivity. "$a \times b$" indicates a spatial partitions in x and b in y, for a total of $a \times b$.

Figure 7 presents the relative angular flux error against the total solve times using ARDPOD. The total solve time is the time to complete the entire adaptive solution process. While the ARDPOD solver is far from optimised, the graphs still show that ARDPOD reduces the angular flux error by up to an order of magnitude for a given solve time when compared to DPOD, and that the error exhibits a modest increase in order of convergence.

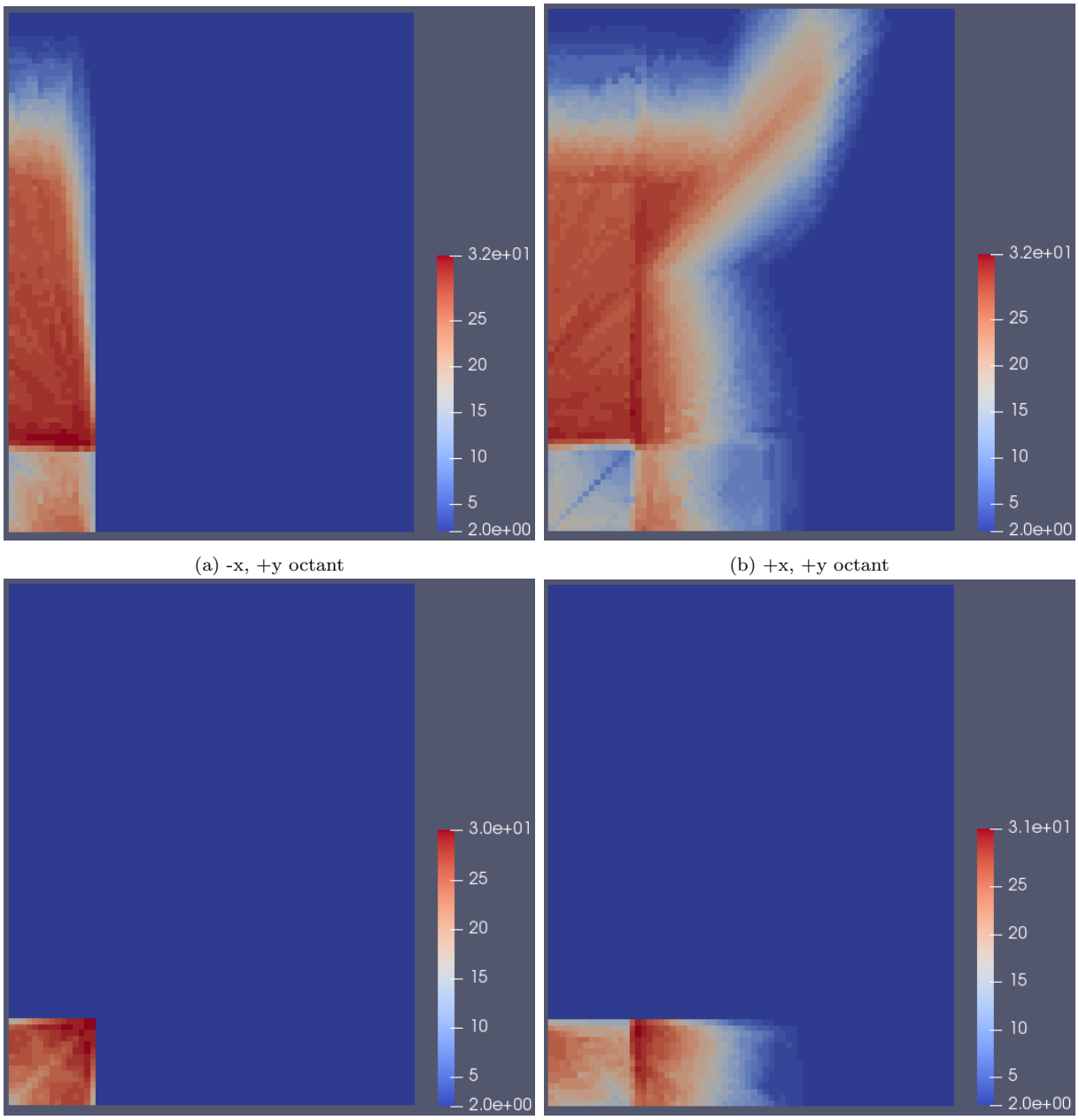

(a) -x, +y octant

(b) +x, +y octant

(c) -x, -y octant

(d) +x, -y octant

Figure 8: The number of ARDPOD basis functions per octant in each spatial region, for the dog-leg duct extrapolation problem, with 70x90 regions and a mean of 84 basis functions per node in total.

Figure 8 shows the number of basis functions associated with each octant in each spatial region, for the dog-leg duct extrapolation problem. The figures show that basis functions have predominantly been added to high flux regions, such as inside the duct and at its borders. This demonstrates that the adaptive method is successfully increasing the resolution in regions where additional basis functions are likely to be most beneficial, and thus explains the method's success in reducing the error for a given number of basis functions.

4.2 The Watanabe-Maynard Problem

The second example is the Watanabe-Maynard problem [50]. Figure 9a depicts a schematic of the spatial domain. Region 1 is the source, region 2 is a void, and region 3 is a moderate absorber and scatterer. Table 2 shows the material properties of each region for the training and test solutions. Reflective boundary conditions are applied to the bottom and left boundaries, and vacuum boundary conditions are applied to the top and right. The spatial domain is discretised with a 160×160 mesh of discontinuous linear quadrilateral elements. The S_{50} angular discretisation was employed to produce full order angular solutions. Figure 9b depicts the scalar flux distribution of the S_{50} solution to the interpolation problem.

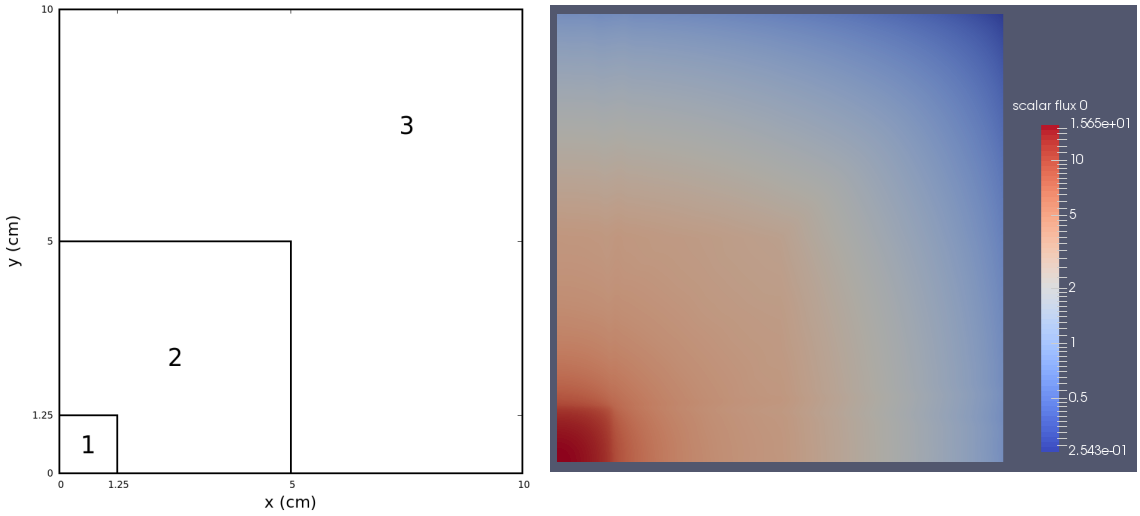

(a) Schematic

(b) S_{50} scalar flux solution

Figure 9: Schematic (a) and S_{50} scalar flux solution (b) for the Watanabe-Maynard interpolation problem. Region 1 is the source, region 2 is a void and region 3 is a moderately absorbing and scattering material.

Table 2 lists the material cross sections for the training and test problems. As previously, the snapshot matrix was formed from all four training solutions, and the resulting bases were used to solve both an interpolation and an extrapolation problem.

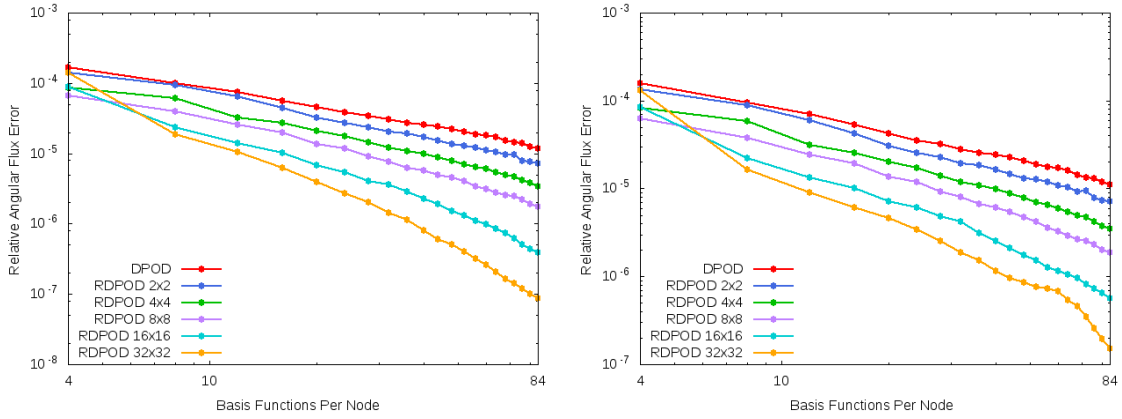

(a) Interpolation (b) Extrapolation

Figure 10: Angular flux error vs number of basis functions for S_{50} solutions to the Watanabe-Maynard problems with varying numbers of spatial regions.

Figures 10a and 10b depict the L^2-norm of the angular flux error for the Watanabe-Maynard problems, for both DPOD and RDPOD with varying numbers of regions. As the figure shows, increasing the number of RDPOD regions consistently reduces the angular flux error for a given basis size, excluding 4 basis functions. With just 8 basis functions, the maximum reduction in error is an order of magnitude, which increases steadily to 2 orders of magnitude by 84 basis functions.

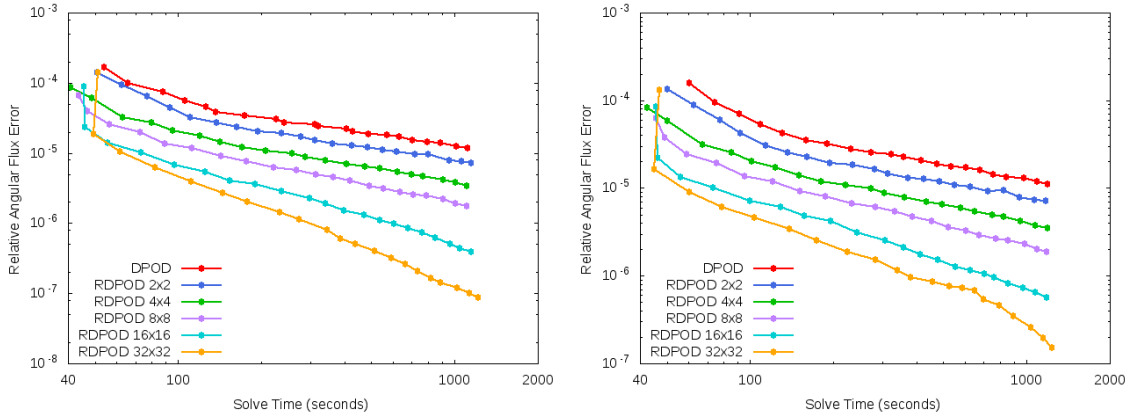

(a) Interpolation (b) Extrapolation

Figure 11: Angular flux error vs solve time in seconds for S_{50} solutions to the Watanabe-Maynard problems with varying numbers of spatial regions. "$a \times b$" indicates a spatial partitions in x and b in y, for a total of $a \times b$.

Figure 11 plots the relative angular flux error against the solve time for DPOD and RDPOD. It is again shown that increasing the number of spatial regions consistently decreases the error for a given solve time, with a maximum reduction of more than 2 orders of magnitude.

In some cases, moving from 4 to 8 basis functions decreased both the error and the solve time, which was not expected. This is likely because the iterative solver converged slowly for the bases with 4 functions, so adding a basis function to each octant not only reduced

the error as expected, but also allowed the solver to converge in fewer iterations and thereby reduced the solve time.

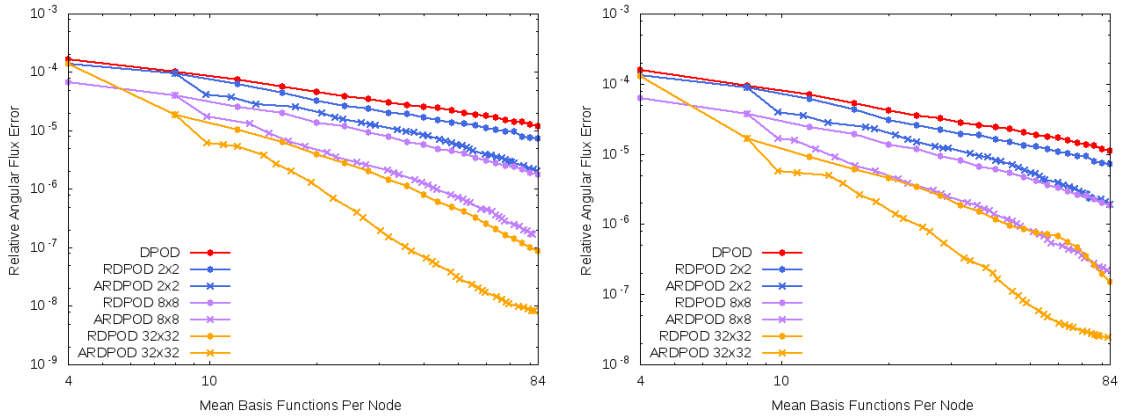

(a) Interpolation (b) Extrapolation

Figure 12: Angular flux error for adaptive S_{50} solutions to the Watanabe-Maynard problems with varying numbers of spatial regions. "$a \times b$" indicates a spatial partitions in x and b in y, for a total of $a \times b$.

Figure 12 plots the relative angular flux error against the mean number of basis functions per node for all three methods with varying numbers of regions. As the figure shows, ARDPOD reduces the error compared to RDPOD in all cases, with a peak reduction of approximately an order of magnitude. Compared to DPOD, ARDPOD reduces the error by approximately 2.5 orders of magnitude. The figure also shows, once again, that increasing the number of regions consistently reduces error for both RDPOD and ARDPOD.

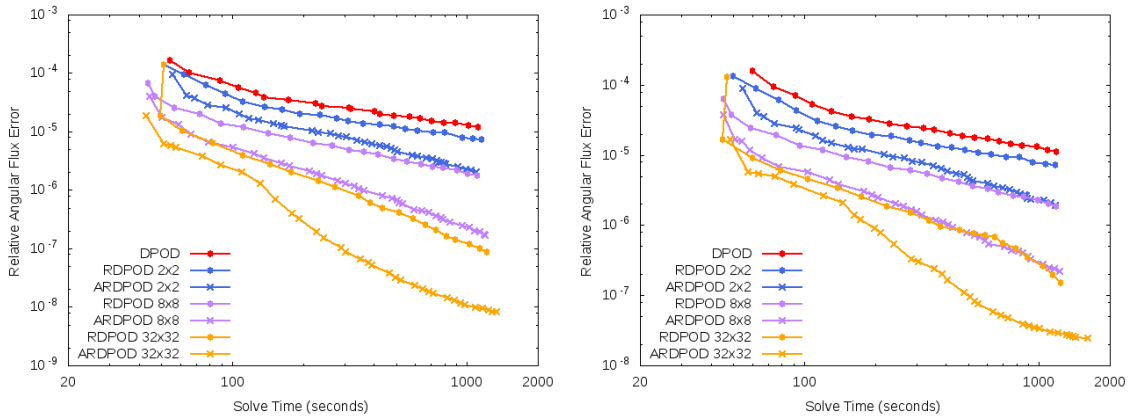

(a) Interpolation (b) Extrapolation

Figure 13: Angular flux error vs solve time in seconds for S_{50} solutions to the Watanabe-Maynard problems with varying numbers of spatial regions using angular adaptivity. "$a \times b$" indicates a spatial partitions in x and b in y, for a total of $a \times b$.

Figure 13 compares the relative angular flux error to the solve times for DPOD, RDPOD and ARDPOD. As explained in the discussion of figure 6, the solve times given are for a single iteration, and are intended to be indicative. The cumulative solve time is not considered,

as the solver has not yet been optimised for this purpose. The figure shows that ARDPOD drastically decreases the error for a given solve time, with a peak reduction of more than 3 orders of magnitude. This demonstrates that, while RDPOD and ARDPOD both reduce error compared to DPOD for a given basis size, they do not significantly affect the solve time. Similar anomalies to figure 11 are seen with 4 basis functions per node, likely for the same reason.

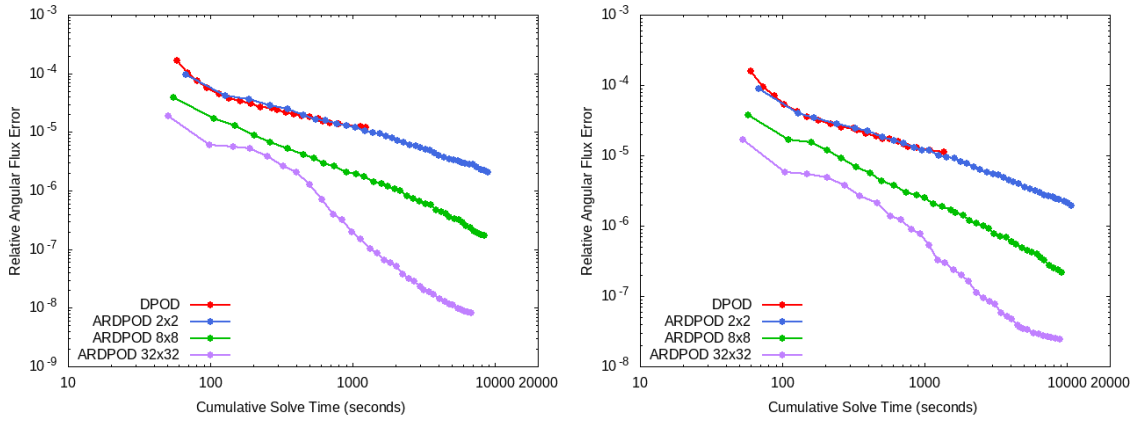

(a) Interpolation

(b) Extrapolation

Figure 14: Angular flux error vs cumulative solve time in seconds for S_{50} solutions to the Watanabe-Maynard problems with varying numbers of spatial regions using angular adaptivity. "$a \times b$" indicates a spatial partitions in x and b in y, for a total of $a \times b$.

Figure 14 presents the relative angular flux error against the cumulative solve time for ARDPOD. As mentioned in the discussion of figure 7, the adaptive method is not yet fully optimised, and significant improvements in this metric are likely possible. Despite this, the graphs show that ARDPOD performs at least as well as DPOD in the case of 2x2 regions, and significantly better with more regions. At best, it offers over an order of magnitude reduction in error with the same solve time as DPOD.

5 Conclusions

This article has developed upon the method of DPOD proposed in a recent article [42]. A new reduced order model for the angular dimension of the Boltzmann transport equation, known as RDPOD, has been described. The novelty of RDPOD lies in its separation of the spatial domain into multiple regions, each of which has its own optimised DPOD basis set. A method of projecting flux between each reduced order basis without full order calculations has also been derived and implemented. Finally, an adaptive algorithm based on the RDPOD bases has been presented.

The RDPOD method is shown to consistently decrease the relative angular flux error for a given solve time and basis size when compared to DPOD, by an amount proportional to the number of spatial regions. This was the expected result, as increasing the number of regions reduces the number of elements per region, and therefore allows each basis function to be better optimised for the angular flux profiles it represents. The relative angular flux error for

a given number of basis functions was reduced by up to an order of magnitude for the dog-leg duct problem, and 2 orders of magnitude for the Watanabe-Maynard problem, demonstrating that the method can benefit both advection and scattering problems. Similar results were observed when comparing the error to the solve time, as RDPOD did not significantly affect the solve time for a given basis size compared to DPOD.

The adaptive method, known as ARDPOD, was demonstrated to further reduce error for a given basis size compared to RDPOD. The effect of adaptivity was significant - for both numerical examples, the error was reduced by up to 3 orders of magnitude compared to DPOD. Compared to RDPOD with the same number of regions, ARDPOD typically reduced the error by up to an order of magnitude, and more in some cases. The same was true when comparing the error to the solve time for each iteration. However, as previously mentioned, the cumulative time to reach a given adaptive stage was not optimised. Additional optimisation of the adaptive method could significantly reduce the cumulative solve time, but this is left for future work.

6 Tables

Problem	Material	Source ($cm^{-2}s^{-1}$)	Σ_a (cm^{-1})	Σ_s (cm^{-1})
1	1	1.00	0.50	0.00
	2	0.00	0.00	0.00
	3	0.00	0.50	0.00
2	1	1.00	1.50	0.00
	2	0.00	0.00	0.00
	3	0.00	1.50	0.00
3	1	1.00	0.50	0.00
	2	0.00	0.05	0.00
	3	0.00	0.50	0.00
4	1	1.00	1.50	0.00
	2	0.00	0.05	0.00
	3	0.00	1.50	0.00
Interpolation	1	1.00	1.00	0.00
	2	0.00	0.025	0.00
	3	0.00	1.00	0.00
Extrapolation	1	1.00	2.00	0.00
	2	0.00	0.10	0.00
	3	0.00	2.00	0.00

Table 1: Material properties for the dog-leg duct solutions. Material 1 is the source, material 2 is the duct, and material 3 is a neutron absorbing material.

Problem	Material	Source ($cm^{-2}s^{-1}$)	Σ_a (cm^{-1})	Σ_s (cm^{-1})
1	1	6.40	0.01	0.19
	2	0.00	0.00	0.00
	3	0.00	0.01	0.19
2	1	6.40	0.01	0.21
	2	0.00	0.00	0.00
	3	0.00	0.01	0.21
3	1	6.40	0.03	0.19
	2	0.00	0.00	0.00
	3	0.00	0.03	0.19
4	1	6.40	0.03	0.21
	2	0.00	0.00	0.00
	3	0.00	0.03	0.21
Interpolation	1	6.40	0.02	0.20
	2	0.00	0.00	0.00
	3	0.00	0.02	0.20
Extrapolation	1	6.40	0.02	0.22
	2	0.00	0.00	0.00
	3	0.00	0.02	0.22

Table 2: Material properties for the Watanabe-Maynard solutions. Material 1 is the source, material 2 is a void, and material 3 is moderately absorbing and scattering.

7 Acknowledgements

The authors wish to acknowledge the funding of this research through the grant EP/M022684/2. This research utilised Queen Mary's Apocrita HPC facility, supported by QMUL Research-IT. http://doi.org/10.5281/zenodo.438045

8 Bibliography

[1] P. Lesaint and P.A. Raviart. "On a Finite Element Method for Solving the Neutron Transport Equation". In: *Publications mathématiques et informatique de Rennes* S4 (1974). DOI: https://doi.org/10.1016/B978-0-12-208350-1.50008-X.

[2] H. Park and C.R.E. de Oliveira. "Coupled Space-Angle Adaptivity for Radiation Transport Calculations". In: *Nuclear Science and Engineering* 161.2 (2009), pp. 216–234. DOI: https://doi.org/10.13182/NSE161-216.

[3] S. Jewer, A.G. Buchan, C.C. Pain, and D.G. Cacuci. "An immersed body method for coupled neutron transport and thermal hydraulic simulations of PWR assemblies". In: *Annals of Nuclear Energy* (2014). ISSN: 03064549. DOI: 10.1016/j.anucene.2013.12.018.

[4] A.G. Buchan, C.C. Pain, M.D. Eaton, R.P. Smedley-Stevenson, and A.J.H. Goddard. "Self-Adaptive Spherical Wavelets for Angular Discretizations of the Boltzmann Transport Equation". In: *Nuclear Science and Engineering* 158.3 (2008), pp. 244–263. DOI: 10.13182/NSE08-A2751. eprint: https://doi.org/10.13182/NSE08-A2751. URL: https://doi.org/10.13182/NSE08-A2751.

[5] J. Kópházi and D. Lathouwers. "A space–angle DGFEM approach for the Boltzmann radiation transport equation with local angular refinement". In: *Journal of Computational Physics* 297 (2015), pp. 637–668. DOI: https://doi.org/10.1016/j.jcp.2015.05.031.

[6] S. Dargaville, R.P. Smedley-Stevenson, P.N. Smith, and C.C. Pain. "Goal-based angular adaptivity for Boltzmann transport in the presence of ray-effects". In: *Journal of Computational Physics* 421 (2020), p. 109759. ISSN: 0021-9991. DOI: https://doi.org/10.1016/j.jcp.2020.109759. URL: https://www.sciencedirect.com/science/article/pii/S0021999120305337.

[7] G. Jiang, H. Liu, K. Yang, and X. Gao. "A fast reduced-order model for radial integral boundary element method based on proper orthogonal decomposition in nonlinear transient heat conduction problems". In: *Computer Methods in Applied Mechanics and Engineering* 368 (2020), p. 113190. ISSN: 0045-7825. DOI: https://doi.org/10.1016/j.cma.2020.113190. URL: https://www.sciencedirect.com/science/article/pii/S0045782520303753.

[8] A. Alomar, A. Nicole, D. Sipp, V. Rialland, and F. Vuillot. "Reduced-order model of a reacting, turbulent supersonic jet based on proper orthogonal decomposition". In: *Theoretical and Computational Fluid Dynamics* (2020), pp. 1–29.

[9] N. El Moçayd, M.S. Mohamed, D. Ouazar, and M. Seaid. "Stochastic model reduction for polynomial chaos expansion of acoustic waves using proper orthogonal decomposition". In: *Reliability Engineering & System Safety* 195 (2020), p. 106733. ISSN: 0951-8320. DOI: https://doi.org/10.1016/j.ress.2019.106733. URL: https://www.sciencedirect.com/science/article/pii/S0951832019303242.

[10] M. Abbaszadeh, M. Dehghan, and I.M. Navon. "A proper orthogonal decomposition variational multiscale meshless interpolating element-free Galerkin method for incompressible magnetohydrodynamics flow". In: *International Journal for Numerical Methods in Fluids* 92.10 (2020), pp. 1415–1436.

[11] D. Huang, J.N. Fuhg, C. Weißenfels, and P. Wriggers. "A machine learning based plasticity model using proper orthogonal decomposition". In: *Computer Methods in Applied Mechanics and Engineering* 365 (2020), p. 113008. ISSN: 0045-7825. DOI: https://doi.org/10.1016/j.cma.2020.113008. URL: https://www.sciencedirect.com/science/article/pii/S0045782520301924.

[12] Q. Wang, J.S. Hesthaven, and D. Ray. "Non-intrusive reduced order modeling of unsteady flows using artificial neural networks with application to a combustion problem". In: *Journal of Computational Physics* 384 (2019), pp. 289–307. ISSN: 0021-9991. DOI: https://doi.org/10.1016/j.jcp.2019.01.031. URL: https://www.sciencedirect.com/science/article/pii/S0021999119300828.

[13] O.r San and R. Maulik. "Neural network closures for nonlinear model order reduction". In: *Advances in Computational Mathematics* 44.6 (Jan. 2018), pp. 1717–1750. DOI: 10.1007/s10444-018-9590-z. URL: http://dx.doi.org/10.1007/s10444-018-9590-z.

[14] Saeed E.A., A. Rageh, and D. Linzell. "Damage detection in structural systems utilizing artificial neural networks and proper orthogonal decomposition". In: *Structural Control and Health Monitoring* 26.2 (2019). e2288 STC-18-0042.R2, e2288. DOI: https://doi.org/10.1002/stc.2288. eprint: https://onlinelibrary.wiley.com/doi/pdf/10.1002/stc.2288. URL: https://onlinelibrary.wiley.com/doi/abs/10.1002/stc.2288.

[15] H. Zhong, Q. Xiong, L. Yin, J. Zhang, Y. Zhu, S. Liang, B. Niu, and X. Zhang. "CFD-based reduced-order modeling of fluidized-bed biomass fast pyrolysis using artificial neural network". In: *Renewable Energy* 152 (2020), pp. 613–626. ISSN: 0960-1481. DOI: https://doi.org/10.1016/j.renene.2020.01.057. URL: https://www.sciencedirect.com/science/article/pii/S0960148120300628.

[16] A.J. Morris J. Zhang. "Fuzzy neural networks for nonlinear systems modelling". English. In: *IEE Proceedings - Control Theory and Applications* 142 (6 Nov. 1995), 551–561(10). ISSN: 1350-2379. URL: https://digital-library.theiet.org/content/journals/10.1049/ip-cta_19952255.

[17] W. Silva. "Identification of nonlinear aeroelastic systems based on the Volterra theory: progress and opportunities". In: *Nonlinear Dynamics* 39.1 (2005), pp. 25–62.

[18] M. Rydel and R. Stanisławski. "A new frequency weighted Fourier-based method for model order reduction". In: *Automatica* 88 (2018), pp. 107–112.

[19] J.W. Bandler, Q.S. Cheng, S.A. Dakroury, A.S. Mohamed, M.H. Bakr, K. Madsen, and J. Sondergaard. "Space mapping: the state of the art". In: *IEEE Transactions on Microwave Theory and Techniques* 52.1 (2004), pp. 337–361. DOI: 10.1109/TMTT.2003.820904.

[20] G. Aversano, A. Bellemans, Z. Li, A. Coussement, O. Gicquel, and A. Parente. "Application of reduced-order models based on PCA & Kriging for the development of digital twins of reacting flow applications". In: *Computers & Chemical Engineering* 121 (2019), pp. 422–441. ISSN: 0098-1354. DOI: https://doi.org/10.1016/j.compchemeng.2018.09.022. URL: https://www.sciencedirect.com/science/article/pii/S0098135418305891.

[21] J. Blahoš, A. Vizzaccaro, L. Salles, and F. El Haddad. "Parallel Harmonic Balance Method for Analysis of Nonlinear Dynamical Systems". In: vol. Volume 11: Structures and Dynamics: Structural Mechanics, Vibration, and Damping; Supercritical CO2. Turbo Expo: Power for Land, Sea, and Air. V011T30A028. Sept. 2020. DOI: 10.1115/GT2020-15392. eprint: https://asmedigitalcollection.asme.org/GT/proceedings-pdf/GT2020/84232/V011T30A028/6617159/v011t30a028-gt2020-15392.pdf. URL: https://doi.org/10.1115/GT2020-15392.

[22] X. Chen, L. Liu, T. Long, and Z. Yue. "A reduced order aerothermodynamic modeling framework for hypersonic vehicles based on surrogate and POD". In: *Chinese Journal of Aeronautics* 28.5 (2015), pp. 1328–1342. ISSN: 1000-9361. DOI: https://doi.org/10.1016/j.cja.2015.06.024. URL: https://www.sciencedirect.com/science/article/pii/S1000936115001697.

[23] J. Eftang, A. Patera, and E. Rønquist. "An "hp" Certified Reduced Basis Method for Parametrized Elliptic Partial Differential Equations". In: *SIAM J. Scientific Computing* 32 (Sept. 2010), pp. 3170–3200. DOI: 10.1137/090780122.

[24] Y. Chen, J. Hesthaven, and Y. Maday. "A Seamless Reduced Basis Element Method for 2D Maxwell's Problem: An Introduction". In: vol. 76. Oct. 2010, pp. 141–152. ISBN: 978-3-642-15336-5. DOI: 10.1007/978-3-642-15337-2_11.

[25] P. Pacciarini, P. Gervasio, and A. Quarteroni. "Spectral based Discontinuous Galerkin Reduced Basis Element method for parametrized Stokes problems". In: *Computers & Mathematics with Applications* 72.8 (2016). Finite Elements in Flow Problems 2015, pp. 1977–1987. ISSN: 0898-1221. DOI: https://doi.org/10.1016/j.camwa.2016.01.030. URL: https://www.sciencedirect.com/science/article/pii/S0898122116300268.

[26] M. Buffoni, H. Telib, and A. Iollo. "Iterative methods for model reduction by domain decomposition". In: *Computers & Fluids* 38.6 (2009), pp. 1160–1167. ISSN: 0045-7930. DOI: https://doi.org/10.1016/j.compfluid.2008.11.008. URL: https://www.sciencedirect.com/science/article/pii/S0045793008002259.

[27] S. Riffaud, M. Bergmann, C. Farhat, . Grimberg, and A. Iollo. "The DGDD method for reduced-order modeling of conservation laws". In: *Journal of Computational Physics* 437 (2021), p. 110336. ISSN: 0021-9991. DOI: https://doi.org/10.1016/j.jcp.2021.110336. URL: https://www.sciencedirect.com/science/article/pii/S002199912100231X.

[28] F. Wols. "Transient analyses of accelerator driven systems using modal expansion techniques". MA thesis. Delft University of Technology, 2010.

[29] J. Coale and D. Anistratov. "Data-Driven Grey Reduced-Order Model for Thermal Radiative Transfer Problems Based on Low-Order Quasidiffusion Equations and Proper Orthogonal Decomposition". In: *Transactions of the American Nuclear Society* 121 (Nov. 2019), pp. 836–839. DOI: 10.13182/T31313.

[30] A.G. Buchan, C.C. Pain, F. Fang, and I.M. Navon. "A POD reduced-order model for eigenvalue problems with application to reactor physics". In: *International Journal for Numerical Methods in Engineering* 95.12 (2013), pp. 1011–1032. DOI: https://doi.org/10.1002/nme.4533.

[31] A.G. Buchan, A.A. Calloo, M.G. Goffin, S. Dargaville, F. Fang, C.C. Pain, and I.M. Navon. "A POD reduced order model for resolving angular direction in neutron/photon transport problems". In: *Journal of Computational Physics* 296 (2015), pp. 138–157. DOI: https://doi.org/10.1016/J.JCP.2015.04.043.

[32] Z. Peng, Y. Chen, Y. Cheng, and F. Li. "A reduced basis method for radiative transfer equation". In: *ArXiv* abs/2103.07574 (2021).

[33] L. Soucasse, A.G. Buchan, S. Dargaville, and C.C. Pain. "An angular reduced order model for radiative transfer in non grey media". In: *Journal of Quantitative Spectroscopy and Radiative Transfer* 229 (2019), pp. 23–32. ISSN: 0022-4073. DOI: https://doi.org/10.1016/j.jqsrt.2019.03.005. URL: https://www.sciencedirect.com/science/article/pii/S0022407319300329.

[34] J. Tencer, K. Carlberg, R. Hogan, and M. Larsen. "Reduced Order Modeling Applied to the Discrete Ordinates Method for Radiation Heat Transfer in Participating Media". In: vol. Volume 2. Heat Transfer Summer Conference. V002T15A011. July 2016. DOI: 10.1115/HT2016-7010. eprint: https://asmedigitalcollection.asme.org/HT/proceedings-pdf/HT2016/50336/V002T15A011/2441960/v002t15a011-ht2016-7010.pdf. URL: https://doi.org/10.1115/HT2016-7010.

[35] D. Huang, H. Abdel-Khalik, C. Rabiti, and F. Gleicher. "Dimensionality reducibility for multi-physics reduced order modeling". In: *Annals of Nuclear Energy* 110 (Dec. 2017), pp. 526–540. ISSN: 0306-4549. DOI: 10.1016/J.ANUCENE.2017.06.045. URL: https://www.sciencedirect.com/science/article/pii/S0306454917301780.

[36] C. Castagna, M. Aufiero, S. Lorenzi, G. Lomonaco, and A. Cammi. "Development of a Reduced Order Model for Fuel Burnup Analysis". In: *Energies* 13.4 (2020). ISSN: 1996-1073. DOI: 10.3390/en13040890. URL: https://www.mdpi.com/1996-1073/13/4/890.

[37] H. Gong, Y. Yu, and Q. Li. "Reactor power distribution detection and estimation via a stabilized gappy proper orthogonal decomposition method". In: *Nuclear Engineering and Design* 370 (2020), p. 110833. ISSN: 0029-5493. DOI: https://doi.org/10.1016/j.nucengdes.2020.110833. URL: https://www.sciencedirect.com/science/article/pii/S0029549320303277.

[38] C. Ghnatios, F. Masson, A. Huerta, A. Leygue, E. Cueto, and F. Chinesta. "Proper Generalized Decomposition based dynamic data-driven control of thermal processes". In: *Computer Methods in Applied Mechanics and Engineering* 213-216 (2012), pp. 29–41. ISSN: 0045-7825. DOI: https://doi.org/10.1016/j.cma.2011.11.018. URL: https://www.sciencedirect.com/science/article/pii/S0045782511003641.

[39] C.E. Heaney, A.G. Buchan, C.C. Pain, and S. Jewer. "Reduced-Order Modelling Applied to the Multigroup Neutron Diffusion Equation Using a Nonlinear Interpolation Method for Control-Rod Movement". In: *Energies* 14.5 (Mar. 2021), p. 1350. ISSN: 1996-1073. DOI: 10.3390/en14051350. URL: http://dx.doi.org/10.3390/en14051350.

[40] G. Helin, C. Wei, Z. Chunyu, and C. Gong. "Fast solution of neutron diffusion problem with movement of control rods". In: *Annals of Nuclear Energy* 149 (2020), p. 107814. ISSN: 0306-4549. DOI: https://doi.org/10.1016/j.anucene.2020.107814. URL: https://www.sciencedirect.com/science/article/pii/S0306454920305120.

[41] T. Phillips, C.E. Heaney, P.N. Smith, and C.C. Pain. "An autoencoder-based reduced-order model for eigenvalue problems with application to neutron diffusion". In: (2020). arXiv: 2008.10532 [math.NA].

[42] A.C. Hughes and A. Buchan. "A discontinuous and adaptive reduced order model for the angular discretization of the Boltzmann transport equation". In: *International Journal for Numerical Methods in Engineering* 121 (2020), pp. 5647–5666.

[43] W.H. Reed and T.R. Hill. "Triangular mesh methods for the neutron transport equation". In: (Oct. 1973).

[44] A.R. Owens, J.A. Welch, J. Kópházi, and M.D. Eaton. "Discontinuous isogeometric analysis methods for the first-order form of the neutron transport equation with discrete ordinate (SN) angular discretisation". In: *Journal of Computational Physics* 315 (2016), pp. 501–535. DOI: https://doi.org/10.1016/j.jcp.2016.03.060.

[45] A.G. Buchan, S.R. Merton, C.C. Pain, and R.P. Smedley-Stevenson. "Riemann boundary conditions for the Boltzmann transport equation using arbitrary angular approximations". In: *Annals of Nuclear Energy* 38.5 (2011), pp. 1186–1195. ISSN: 0306-4549. DOI: https://doi.org/10.1016/j.anucene.2010.11.019. URL: https://www.sciencedirect.com/science/article/pii/S0306454910004081.

[46] L. Sirovich. "Turbulence and the dynamics of coherent structures". In: *Quarterly of Applied Mathematics* 5 (1987), pp. 561–590. DOI: https://doi.org/10.1090/qam/910462.

[47] E.E. Lewis and W.F. Miller. *Computational methods of neutron transport*. John Wiley and Sons, Inc., New York, NY, Jan. 1984. URL: https://www.osti.gov/biblio/5538794.

[48] Thomas M. Evans, Alissa S. Stafford, Rachel N. Slaybaugh, and Kevin T. Clarno. "Denovo: A New Three-Dimensional Parallel Discrete Ordinates Code in SCALE". In: *Nuclear Technology* 171.2 (2010), pp. 171–200. DOI: 10.13182/NT171-171. eprint: https://doi.org/10.13182/NT171-17. URL: https://doi.org/10.13182/NT171-171.

[49] A.G. Buchan, C.C. Pain, M.D. Eaton, R.P. Smedley-Stevenson, and A.J.H. Goddard. "Linear and quadratic octahedral wavelets on the sphere for angular discretisations of the Boltzmann transport equation". In: *Annals of Nuclear Energy* 32.11 (2005), pp. 1224–1273. DOI: https://doi.org/10.1016/j.anucene.2005.01.005.

[50] Y. Watanabe and C.W. Maynard. "The discrete cones method for two-dimensional neutron transport calculations". In: *Transport Theory and Statistical Physics* 15.1-2 (1986), pp. 135–156. DOI: https://doi.org/10.1080/00411458608210448.